JATIS Journal of Astronomical Telescopes, Instruments, and Systems

RESEARCH PAPER

Electro-optical characterization of a CMOS image sensor optimized for soft x-ray astronomy

Charles Townsend-Rose,[a,*] Thomas Buggey,[a] James Ivory,[a] Konstantin D. Stefanov,[a] Lawrence Jones,[a] Oliver Hetherington,[a] Andrew D. Holland,[a] and Thibaut Prod'homme[b]

[a]The Open University, Centre for Electronic Imaging, Milton Keynes, United Kingdom
[b]European Space Agency, ESTEC, Noordwijk, The Netherlands

ABSTRACT. CIS221-X is a prototype complementary metal-oxide-semiconductor (CMOS) image sensor, optimized for soft x-ray astronomy and developed for the proposed ESA Transient High Energy Sky and Early Universe Surveyor (THESEUS) mission. The sensor features 40 μm pitch square pixels built on a 35 μm thick, high-resistivity epitaxial silicon that is fully depleted by reverse substrate bias. Backside illumination processing has been used to achieve high x-ray quantum efficiency, and an optical light-blocking filter has been applied to mitigate the influence of stray light. A comprehensive electro-optical characterization of CIS221-X has been completed. The median readout noise is 3.3 e^-RMS with 90% of pixels reporting a value <3.6 e^-RMS. At −40°C, the dark current is 12.4 ± 0.06 e^-/pixel/s. The pixel photo-response is linear to within 1% for 0.3 to 5 keV photons (82 to 1370 e^-) with <0.1% image lag. Following per-pixel gain correction, an energy resolution of 130.2 ± 0.4 eV has been measured at 5898 eV. In the 0.3 to 1.8 keV energy range, CIS221-X achieves >80% quantum efficiency. With the exception of dark current, these results either meet or outperform the requirements for the THESEUS mission, strongly supporting the consideration of CMOS technology for soft x-ray astronomy.

Keywords: complementary metal-oxide-semiconductor image sensor; soft x-ray astronomy; x-ray detectors; quantum efficiency

Paper 23071G received Jun. 29, 2023; revised Sep. 19, 2023; accepted Sep. 27, 2023; published Oct. 14, 2023.

1 Introduction

Traditionally, the charge-coupled device (CCD) has been the preferred image sensor for soft x-ray astronomy, employed in missions such as XMM-Newton,[1] Chandra,[2] and SMILE.[3] However, more recently, complementary metal-oxide-semiconductor (CMOS) image sensors have been developed specifically for soft x-ray applications.[4] In comparison to CCDs, a CMOS image sensor (CIS) can offer several significant advantages, including faster readout rates, higher operating temperatures and greater radiation hardness. These advantages have lead to the consideration of CIS technology for planned and proposed soft x-ray space missions, including the Einstein Probe[5] and Transient High Energy Sky and Early Universe Surveyor (THESEUS).[6]

THESEUS is a proposed ESA Cosmic Vision M7 mission to monitor the whole sky for high energy transients, particularly gamma-ray bursts. The spacecraft design includes three science instruments: Soft X-ray Imager (SXI), X/Gamma-rays Imaging Spectrometer (XGIS), and InfraRed Telescope (IRT). Early in the mission development, it was identified that the spacecraft

*Address all correspondence to Charles Townsend-Rose, charles.townsend-rose@open.ac.uk

would not be capable of cooling the SXI focal plane to the low temperatures necessary for the use of CCDs.[7] This is a consequence of the orbital properties of the mission, which involve occasional transits through the South Atlantic Anomaly. During these repeated orbits over the course of the 3-year mission, the estimated end-of-life proton fluence for the SXI detectors is 1.55×10^9 p^+ (60 MeV)/cm^2. To mitigate the impact of radiation damage in CCDs, it is necessary that they are operated at temperatures in the range −60°C to −100°C or lower. The SXI focal plane would only be cooled to temperatures in the range −30°C to −40°C, ruling out the use of CCDs and motivating the development of a CIS alternative.

CIS221-X is a prototype CIS, optimized for soft x-ray astronomy and developed for the proposed THESEUS mission.[8] Following the characterization of the frontside-illuminated (FSI) devices[9] and early measurements of the backside-illuminated (BSI) sensors,[10] a comprehensive electro-optical characterization of the BSI CIS221-X has now been completed.

2 CIS221-X

CIS221-X is a 4T pinned photodiode (PPD) CIS based on the readout architecture of Teledyne e2v's Capella CIS120.[11] The pixels are built on 35 μm thick, high-resistivity epitaxial silicon which has undergone BSI processing. The 2048×2048 pixel array is split into four equally sized regions: three variants of 40 μm pitch square pixels and one 10 μm pitch square pixel array. The block diagram of CIS221-X is shown in Fig. 1. An optical-light blocking filter (OBF) has been applied to half of the image area, covering half of each pixel region.

All CIS221-X pixels use a PPD and feature deep depletion extension (DDE) implants, facilitating full/over depletion by reverse substrate bias.[12] The 40 μm pixel variants have an additional pinning implant. As shown in Fig. 2, additional pinning concentrates the charge packet toward the transfer gate during integration, reducing image lag. Despite this provision, initial characterization of the FSI CIS221-X found that "Variant #1" and "Variant #2" of the 40 μm pixels suffered from excessive lag.[9] This was absent in "Variant #3" where the pixels also feature a larger transfer gate.

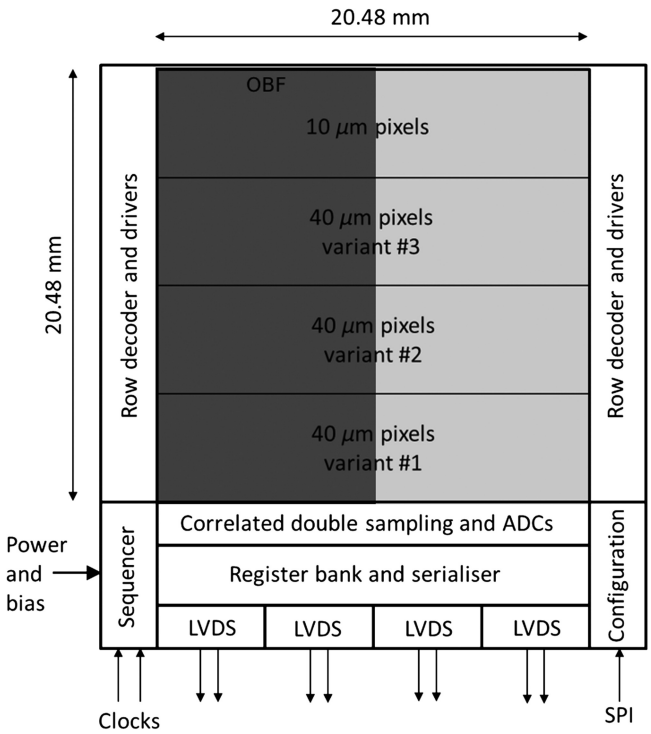

Fig. 1 Block diagram of CIS221-X.

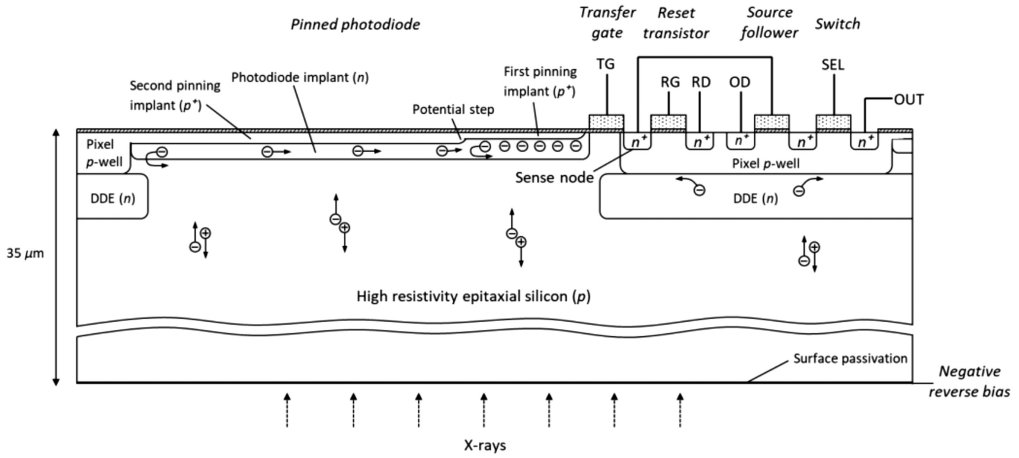

Fig. 2 Simplified cross section diagram of a CIS2221-X 40 μm pixel (not to scale). The second pinning implant concentrates charge toward the transfer gate during integration, reducing image lag.

3 Results and Discussion

The following is focused on the performance of the CIS221-X "Variant #3" 40 μm pixel. All results were measured using one BSI CIS221-X (SN: 21094-07-23) and validated using an identical device (SN: 21094-07-03). Data collection was conducted under vacuum ($\leq 10^{-5}$ hPa) with the detector cooled to −40°C. A reverse bias of −20 V was applied to the detector substrate, ensuring over-depletion.[10] All testing was conducted using an experimental setup[9] at the Centre for Electronic Imaging except the quantum efficiency, which was measured at the BESSY II synchrotron radiation source (Helmholtz-Zentrum Berlin). A conversion gain (see Sec. 3.5) of 10.41 ± 0.005 eV/ADU and a silicon ionization energy of 3.67 eV[13] has been used throughout the analysis. For all results that include an error, the error value has been determined either by calculating 1 standard deviation of the data distribution or, in cases where the distribution has been fit to a Gaussian, by using 1 standard deviation of the corresponding parameter estimate.

3.1 Readout Noise

A set of 50 dark frames were collected and the per-pixel standard deviation was computed to obtain a measurement of the readout noise. The whole device was read out with a minimal integration time of 0.2 s. The contribution from dark current can be suppressed by setting the transfer gate voltage (V_{TG}) to zero, prohibiting charge transfer from the PPD to the sense node. The measured readout noise distribution is presented in Fig. 3. With the dark current suppressed, the median readout noise is 3.3 e^-RMS with 90% of pixels reporting a value <3.6 e^-RMS. This is within the SXI requirement of <5 e^-RMS. Including the contribution from dark current over the minimal integration time (0.2 s), the readout noise is 4.2 e^-RMS at −40°C.

3.2 Dark Current

With the image sensor in darkness, four sets of images were taken at increasing integration times. Using the mean pixel values for each set, the per-pixel dark current was calculated. Figure 4(a) shows large scale non-uniformity in the dark current performance across the image sensor. There is a "glow" coming from the outer column edges of the image area and the bottom row edge where it connects to the 10 μm pixel variant region. This "glow" extends further within the region of the image area that is not covered by the OBF. Also visible is an offset between the background dark current values of the OBF and non-OBF halves of the sensor, as well as a number of hot pixels across the whole image area.

These results are further illustrated by the dark current distributions shown in Fig. 4(b). The "glow" can be seen in the very long tails of the OBF/non-OBF histograms (black). To probe the background dark current within the two halves of the image area, 50 × 50 pixel regions were selected far from the "glow." The respective histograms (red) have much shorter tails, indicating the effect of the "glow" has been minimized though hot pixels are still present.

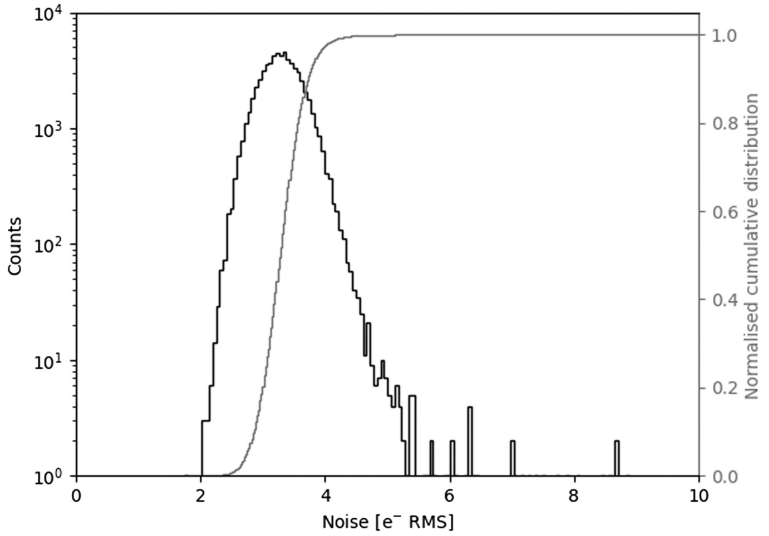

Fig. 3 CIS221-X readout noise distribution with dark current suppressed.

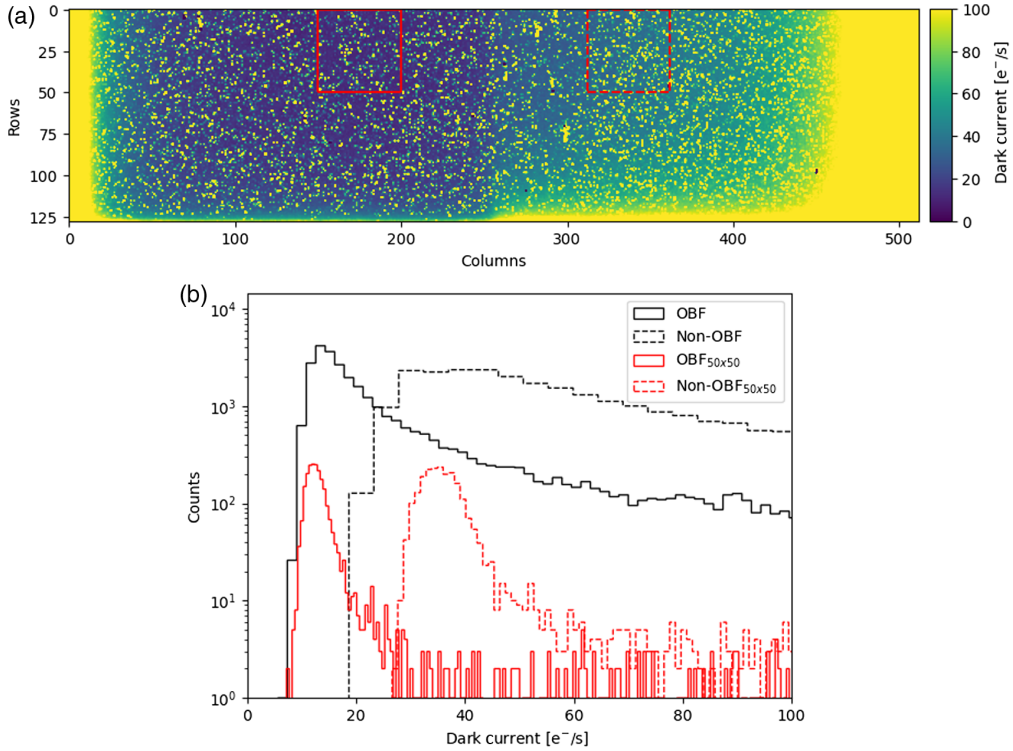

Fig. 4 (a) CIS221-X dark current map with the $OBF_{50\times50}$ and non-$OBF_{50\times50}$ pixel regions outlined (red). (b) Dark current distributions of the whole OBF and non-OBF image areas (black) and the $OBF_{50\times50}$ and non-$OBF_{50\times50}$ pixel regions (red). Dark current data were collected with the image sensor cooled to −40°C.

To exclude the impact of the hot pixels in the measurement, the distributions were fit to a Gaussian function. The corresponding mean dark currents are 12.4 ± 0.06 $e^-/pixel/s$ ($OBF_{50\times50}$) and 35.2 ± 0.09 $e^-/pixel/s$ (non-$OBF_{50\times50}$). This is unexpectedly high for a PPD pixel and exceeds the beginning-of-life THESEUS requirement of <10 $e^-/pixel/s$ at −40°C.

An explanation for the larger than anticipated dark current, the offset between the OBF and non-OBF halves of the image area and the "glow" are not provided here but are subject to an on-going investigation.

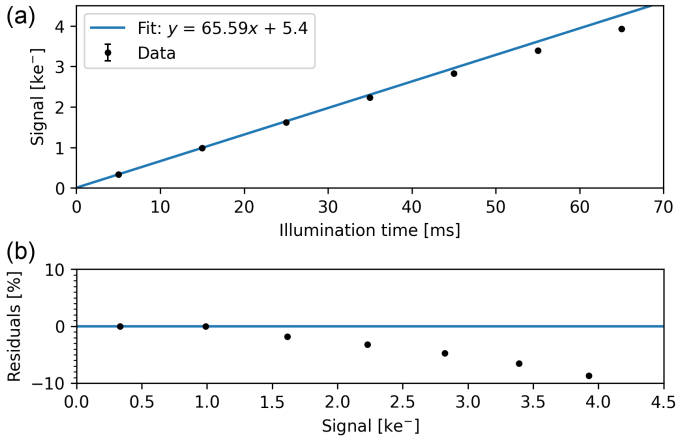

Fig. 5 (a) CIS221-X photo-response measured at −40°C fit to a straight line and (b) the corresponding residuals.

3.3 Non-Linearity

The pixel photo-response was assessed using a light-emitting diode (LED). Sets of images were collected with the integration time fixed and the illumination time (LED "ON" time) varied. The signal generated by the pulsed LED was stable to within ± 4 e$^-$. To ensure statistical accuracy, at least 40 images were collected for each illumination time. Figure 5 shows the mean signal measured for increasing illumination time. Fitting the linear portion of the slope to a straight line and calculating the residuals provides a measure of the non-linearity. For the energy range 0.3 to 5 keV (82 to 1370 e$^-$), the non-linearity is <1%, meeting the SXI requirement.

3.4 Image Lag

The incomplete transfer of charge from the PPD to the sense node during readout is known as image lag. While continuously collecting frames of a fixed integration time, a LED was triggered off for five frames and then on for five frames. The first of the five LED "ON" frames records less signal than the other four and provides a measurement of the lag. Figure 6(a) shows the resultant mean leading-edge image lag as a percentage of signal. At least eight sets of images were collected for each signal to ensure statistical accuracy in spite of any LED instability. For comparison, the lag performance of the CIS221-X "Variant #1" and "Variant 2" pixels are presented alongside that of "Variant #3" (the subject of discussion so far). As measured previously in an FSI device,[9] "Variant #1" and "Variant #2" exhibit excessive lag while "Variant #3" has near-zero lag (<0.1%) for all signal values used. This can be attributed to the larger transfer gate in this variant.

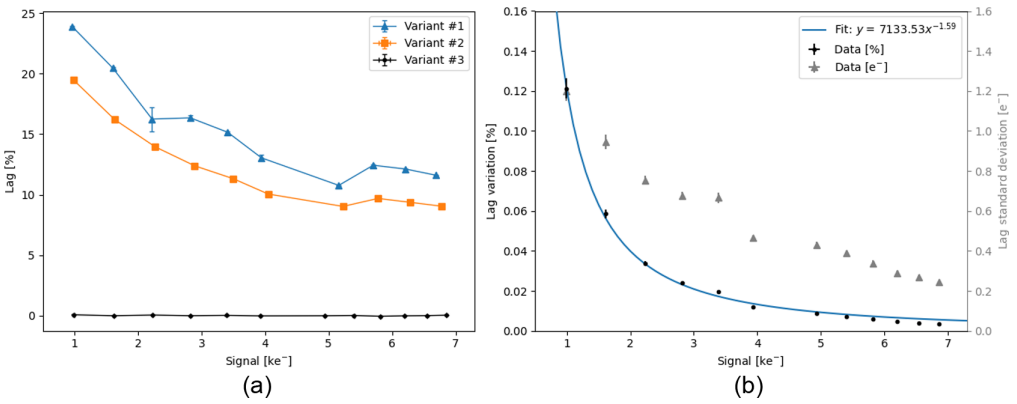

Fig. 6 (a) Mean leading-edge image lag of the CIS221-X "Variant #1," "Variant #2," and "Variant #3" 40 μm pixels expressed as a percentage of signal. (b) CIS221-X "Variant #3" lag variation (fit to a power law function) and standard deviation against signal.

Though the "Variant #3" average image lag is near-zero, each pixel of the image area has a distinct lag value which may vary significantly from the mean. The standard deviation of the per-pixel lag values is shown in Fig. 6(b). Also shown is the lag variation (calculated as the standard deviation divided by the mean signal) which has been fit to a power law function, showing significant variation at low signal which rapidly decreases as the signal increases. This will result in a degraded energy resolution at lower photon energies.

3.5 Per-Pixel Gain

The CIS221-X was exposed to x-ray fluorescence using an x-ray tube and a Mn target. The resultant spectral response is shown in Fig. 7, revealing the $\mathrm{Mn}-\mathrm{K}_{\alpha}$, $\mathrm{Mn}-\mathrm{K}_{\beta}$ emission lines as well as other spectral features originating from the aluminum target support and the vacuum chamber walls. Measuring the position of the $\mathrm{Mn}-\mathrm{K}_{\alpha}$ peak in ADU gives a conversion gain of 10.41 ± 0.005 eV/ADU.

Since each CIS221-X pixel has its own amplifier, each pixel also has a distinct conversion gain. If a sufficient number of x-ray events are recorded by each pixel, the per-pixel gain can be calculated according to the method outlined above. Using 10,000 x-ray exposures with an integration time of 1 s, the per-pixel gain was measured for the whole image area. The measurement error for each pixel is ~0.01 eV/ADU (~0.001%). Figure 8(a) shows non-uniformity in gain at both small and large scales. Most noticeably, the gain is higher at the outer columns of the image area, especially for the non-OBF region.

The large scale non-uniformity is reflected in Fig. 8(b) and the shoulder of values around 11 eV/ADU in the OBF and non-OBF histograms (black). Comparing these two distributions reveals an offset in their per-pixel gains. Examining the same 50×50 pixel regions (red) as defined in Sec. 3.2, the gain variation is $0.64 \pm 0.003\%$ ($\mathrm{OBF}_{50\times50}$) and $0.67 \pm 0.001\%$ ($\mathrm{non\text{-}OBF}_{50\times50}$). The tails of the histograms can be attributed to hot pixels and have been excluded in the measurement by fitting the distributions to Gaussian functions.

The cause of the higher gain in the outer columns and the offset between the OBF and non-OBF regions has not yet been determined. A possible explanation is that the dark current non-uniformity (see Sec. 3.2) is influencing the gain measurement. Section 3.3 shows that the CIS221-X non-linearity grows with increasing signal, which implies the gain would also behave non-linearly. The non-uniformity of the dark current means that the gain is measured at different signal values for each pixel. It would therefore be expected that the per-pixel gain distribution would reflect the same non-uniformity as the dark current, as shown in Fig. 8(a). This possible explanation could be validated by repeating the per-pixel gain measurement as above using a lower integration time, minimizing the influence of dark current.

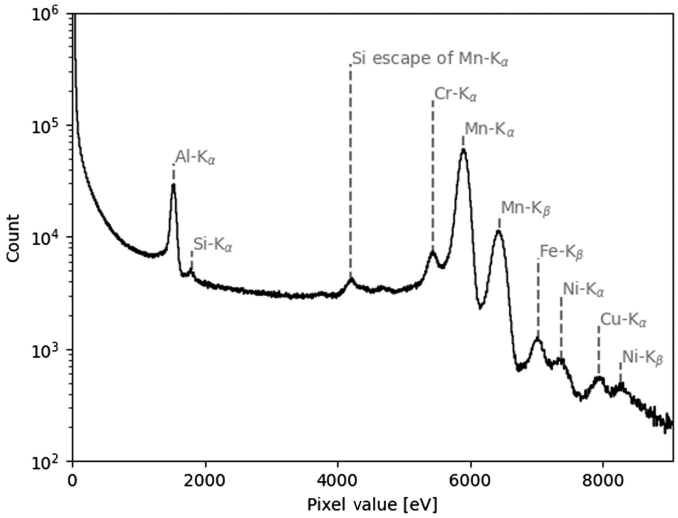

Fig. 7 CIS221-X spectral response to x-ray fluorescence of a Mn target.

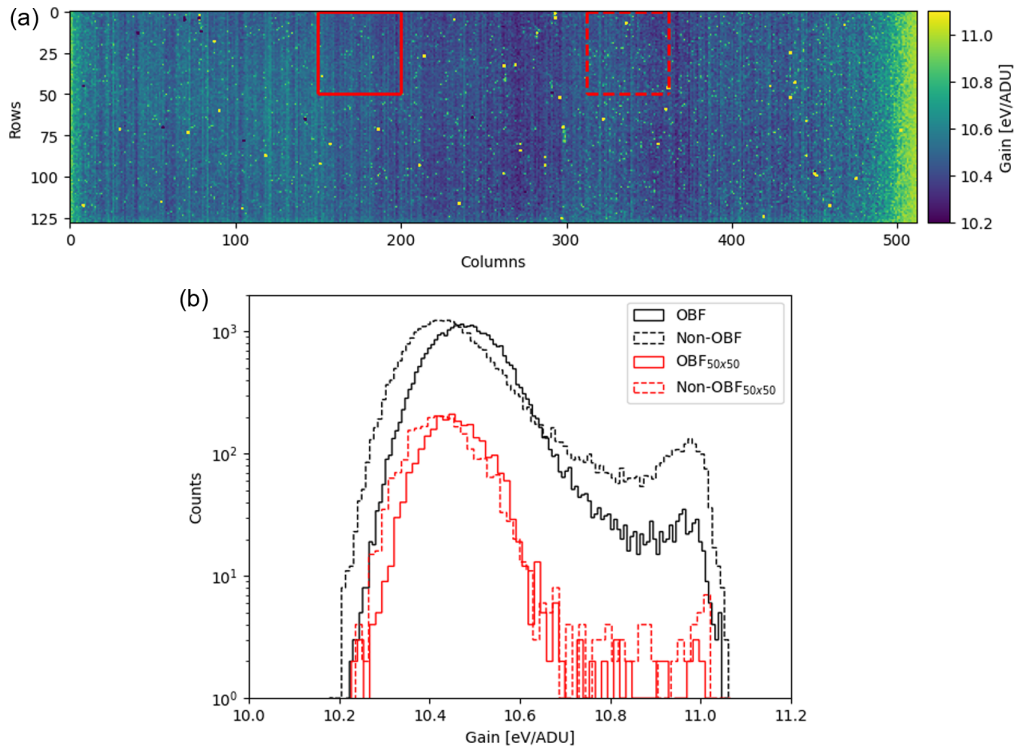

Fig. 8 (a) CIS221-X gain map with the $OBF_{50\times50}$ and non-$OBF_{50\times50}$ pixel regions outlined (red). (b) Gain distributions of the whole OBF and non-OBF image areas (black) and the $OBF_{50\times50}$ and non-$OBF_{50\times50}$ pixel regions (red).

3.6 Energy Resolution

Energy resolution is an important x-ray image sensor parameter and is often used as a benchmark for performance. The energy resolution of a CIS can be expressed as[14]

$$\mathrm{FWHM} = 2.355\omega\sqrt{\frac{FE}{\omega} + \left(\frac{\sigma_{\mathrm{gain}}E}{\omega}\right)^2 + \sigma_{\mathrm{total}}^2}, \tag{1}$$

where ω is the silicon ionization energy (3.67 eV at −40°C[13]), F is the Fano factor (0.12[13]), E is the incident photon energy, σ_{gain} is the gain variation, and σ_{total} is the total noise.

Experimentally, energy resolution is measured as the full width half maximum (FWHM) at a specific spectral peak. When measuring the CIS221-X energy resolution, hot pixels were first excluded using a mask derived from the dark current map (see Sec. 3.2). Then, the x-ray events were graded according the XMM-Newton/EPIC grading procedure[15] and all but the single-pixel events were discarded. This reduced the impact of charge sharing between pixels. The resultant spectrum was fit to a Gaussian function and the energy resolution was calculated as

$$\mathrm{FWHM} = 2.355\sigma, \tag{2}$$

where σ is the standard deviation of the spectral peak.

After measuring the per-pixel gain (see Sec. 3.5), it is possible to correct for the gain variation before measuring the energy resolution. As shown in Fig. 9, this results in a smaller FWHM. Before correction, the CIS221-X energy resolution at the $\mathrm{Mn} - \mathrm{K}_\alpha$ emission line (5898 eV) is 161.7 ± 0.7 eV, while after correction it is 130.2 ± 0.4 eV.

To examine the energy resolution at different photon energies, the image sensor was exposed to x-ray fluorescence of Al (1487 eV), Ti (4510 eV), Mn (5898 eV), and Cu (8047 eV) targets. The corresponding FWHMs are shown in Fig. 10 alongside the Fano limit and the theoretical energy resolution according to Eq. (1). The data before and after per-pixel gain correction are well modeled by Eq. (1) with $\sigma_{\mathrm{gain}} = 0.64\%$ and $\sigma_{\mathrm{gain}} = 0\%$, respectively, validating the per-pixel gain measurement and correction. The total noise was calculated

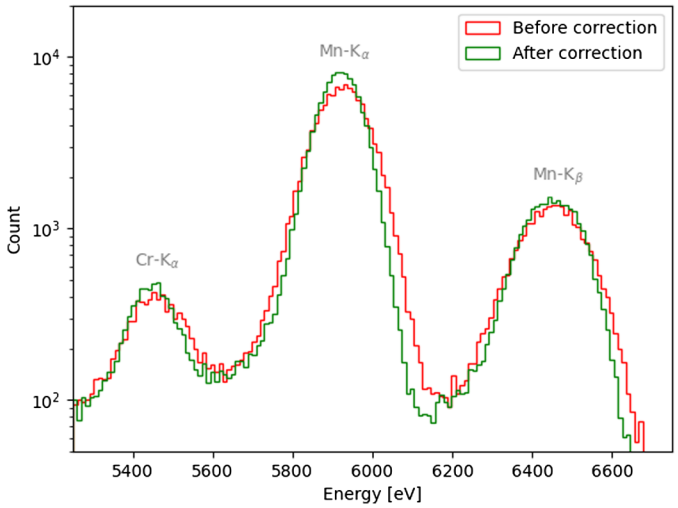

Fig. 9 CIS221-X single-pixel event spectra using a Mn target before and after per-pixel gain correction.

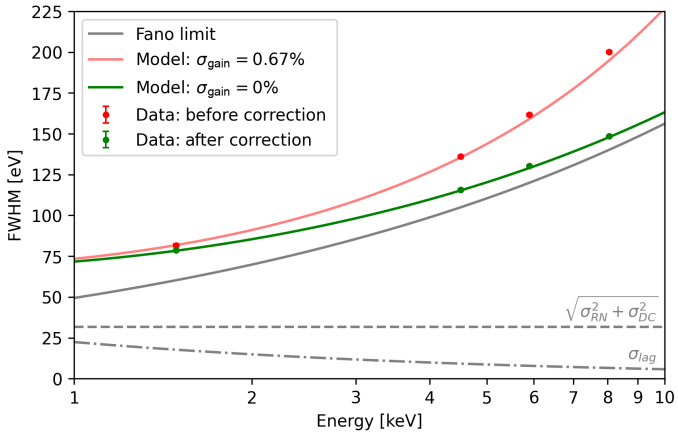

Fig. 10 CIS221-X energy resolution as measured at the Al (1487 eV), Ti (4510 eV), Mn (5898 eV), and Cu (8047 eV) emission peaks. Also shown is the Fano limit and the theoretical energy resolution based on measured CIS221-X noise performance at −40°C.

$$\sigma^2_{\text{total}} = \sigma^2_{\text{RN}} + \sigma^2_{\text{DC}} + \sigma^2_{\text{lag}} + \sigma^2_{\text{other}}, \tag{3}$$

with $\sigma_{\text{RN}} = 3.3$ e$^-$RMS (Sec. 3.1), $\sigma_{\text{DC}} = 1.57$ e$^-$ for a 0.2 s integration time (Sec. 3.2) and σ_{lag} derived using a power law fit to the lag variation (Sec. 3.4). To accurately model the data, it was necessary to include an additional noise component $\sigma_{\text{other}} = 4$ e$^-$, the origin of which is not yet understood but is currently being investigated.

3.7 Quantum Efficiency

The image sensor's quantum efficiency (QE) was measured using the PTB Laboratory at the BESSY II synchrotron radiation source (Helmholtz-Zentrum Berlin). The OBF and non-OBF sides of the device were illuminated separately, and the recorded signal was assessed against a well characterized reference diode. Figure 11 shows the measured QE at various photon energies alongside a layer-model based on an approximate understanding of the image sensor and OBF material compositions. Across the measured energy range, the model fits the data well and the QE performance is as expected. Importantly, the OBF pixels report a QE $> 70\%$ for 0.5 to 1.8 keV photons, outperforming the SXI OBF pixel requirement of $>60\%$ for 0.5 to 1.5 keV. The non-OBF pixels report a QE $> 80\%$ for 0.3 to 1.8 keV, matching the non-OBF pixel requirement

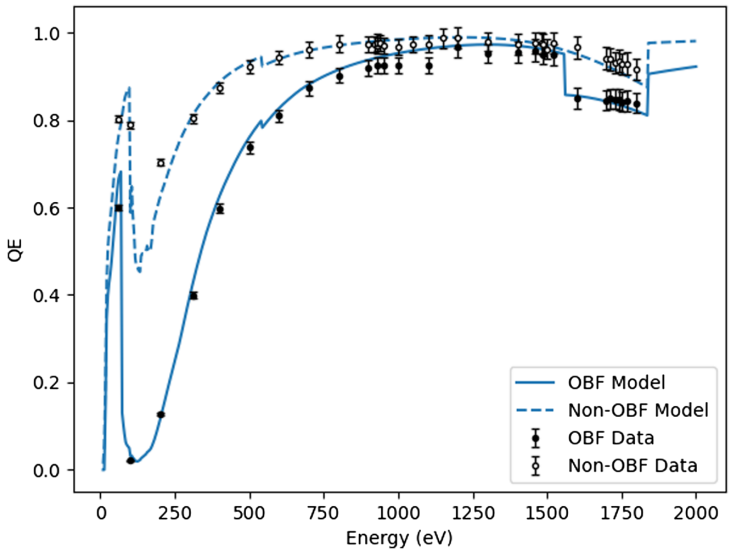

Fig. 11 CIS221-X quantum efficiency at different photon energies alongside a layer-model based on an approximate understanding of image sensor/OBF material composition.

for the energy range measured. However, further testing up to a photon energy of 5 keV is necessary to fully confirm whether the non-OBF pixels meet the SXI QE requirement.

4 Conclusions

A comprehensive electro-optical characterization of the first iteration of a new generation of x-ray optimized CISs, the BSI CIS221-X, has been completed. With the dark current suppressed, the median readout noise is 3.3 e^-RMS with 90% of pixels reporting a value <3.6 e^-RMS. Inclusive of the contribution from the dark current at −40°C over the minimal integration time (0.2 s), the readout noise is 4.2 e^-RMS. In the OBF covered half of the image sensor, the dark current is 12.4 ± 0.06 e^-/pixel/s at −40°C. The pixel photo-response is linear to within 1% for 0.3 to 5 keV photons (82 e^- to 1370 e^-) with <0.1% image lag. Following per-pixel gain correction, an energy resolution of 130.2 ± 0.4 eV has been measured at 5898 eV. In the 0.5 to 1.8 keV energy range, CIS221-X OBF pixels achieve >70% quantum efficiency while the non-OBF pixels report >80% for 0.3 to 1.8 keV. With the exception of dark current, these results either meet or outperform the requirements for the THESEUS SXI instrument. The high and variable dark current will be addressed through process changes in the next iteration of devices.

Earlier this year, the CIS221-X quantum efficiency was measured up to 5 keV. To assess the radiation hardness of the CIS221-X, total-ionizing dose testing has also been completed, the results of which are currently being prepared for publication. Total-non-ionizing dose testing is planned for late 2023.

Code, Data, and Materials Availability

The data that support the findings of this article are not publicly available. They can be requested from the corresponding author at the above-listed email address.

Acknowledgments

This programme was funded by ESA under the E/0901-01 Technology Development Element "CMOS Image Sensor for X-ray Applications." There are no conflicts of interest to declare.

References

1. M. J. L. Turner et al., "The European photon imaging camera on XMM-Newton: the MOS cameras," *A&A* **365**(1), L27–L35 (2001).
2. G. P. Garmire et al., "Advanced CCD imaging spectrometer (ACIS) instrument on the Chandra X-ray Observatory," *Proc. SPIE* **4851**, 28–44 (2003).

3. M. Soman et al., "The SMILE soft x-ray imager (SXI) CCD design and development," *J. Instrum.* **13**, C01022 (2018).
4. Q. Wu et al., "X-ray performance of a customized large-format scientific CMOS detector," *Publ. Astron. Soc. Pac.* **134**, 035006 (2022).
5. W. Yuan et al., "Einstein probe: a lobster-eye telescope for monitoring the x-ray sky," *Proc. SPIE* **10699**, 1069925 (2018).
6. L. Amati et al., "The THESEUS space mission: updated design, profile and expected performances," *Proc. SPIE* **11444**, 114442J (2021).
7. M. McHugh et al., "Development of an imaging system for the THESEUS SXI instrument," *Proc. SPIE* **11444**, 114448Y (2020).
8. J. Heymes et al., "Development of a photon-counting near-fano-limited x-ray CMOS image sensor for THESEUS' SXI," *Proc. SPIE* **11454**, 114540I (2020).
9. J. Heymes et al., "Characterisation of a soft x-ray optimised CMOS image sensor," *J. Instrum.* **17**, P05003 (2022).
10. K. D. Stefanov et al., "A CMOS image sensor for soft x-ray astronomy," *Proc. SPIE* **12191**, 121910N (2022).
11. P. Jorden et al., "Teledyne e2v sensors optimised for ground-based and space applications," *Proc. SPIE* **10709**, 1070903 (2018).
12. K. D. Stefanov et al., "Design and performance of a pinned photodiode CMOS image sensor using reverse substrate bias," *Sensors* **18**(2), 118 (2018).
13. B. Lowe and R. Sareen, "A measurement of the electron-hole pair creation energy and the Fano factor in silicon for 5.9 keV x-rays and their temperature dependence in the range 80-270K," *Nucl. Instrum. Methods Phys. Res. Sec. A Accel. Spectrom. Detect. Assoc. Equip.* **576**(2), 367–370 (2007).
14. Q. Wu et al., "Improving the x-ray energy resolution of a scientific CMOS detector by pixel-level gain correction," *Publ. Astron. Soc. Pac.* **135**, 025003 (2023).
15. "XMM-Newton users handbook", Issue 2.21, ESA: XMM-Newton SOC (2023).

Biographies of the authors are not available.